सीएसआईआर
CSIR
भारत का नवाचार इंजन
The Innovation Engine of India

Indian Journal of Engineering & Materials Sciences
Vol. 33, February 2026, pp. 100-110
DOI: 10.56042/ijems.v33i01.22686

NIScPR
National Institute of Science Communication and Policy Research
सीएसआईआर–निस्पर

Design and performance analysis of novel coaxial magnetic gear using subdomain method

Amberbir Wondimu[a*], Yang Chaojun[a, b, c], Wang Ao[a], Sun Haobo[a] & Gao Yuan[a]

[a]School of Mechanical Engineering, Jiangsu University, Zhenjiang 212013, China
[b]State Key Laboratory of Mechanical Transmission for Advanced Equipment, Chongqing University, Chongqing 400044, China
[c]School of Mechanical Engineering, Nantong Institute of Technology, Nantong 226601, China

Received: 13 August 2025; accepted: 20 January 2026

This paper has introduced an innovative coaxial magnetic gear (CMG) design that has addressed limitations in volume, weight, magnetic losses, and corrosion in conventional CMGs by strategically segmenting permanent magnets and incorporating electrical steel sheet supports within a comb-shaped outer yoke. An inverted T-shaped pole piece has been introduced to enhance the magnetic field. To analyze the CMG, it has been divided into five subdomains, and an analytical method employing Laplace and Poisson equations, along with boundary and continuity conditions, has been used to derive the magnetic field and torque equations. The proposed model has been validated against finite element analyses using the Maxwell stress tensor, which has demonstrated excellent agreement. Furthermore, the design has been verified by comparing it with an equivalent existing CMG model in a small-scale wind turbine application. The results have shown a 3.2% increase in magnetic flux density and a 2.06% increase in magnetic torque. These improvements have highlighted the potential for the proposed CMG design to advance the application of electrical machines in modern engineering solutions.

Keywords: Coaxial magnetic gear, Laplace’s equation, Poisons equation, Subdomain method

1 Introduction

Magnetic gears offer a non-contact electromagnetic torque transmission solution based on the interactions of magnetic fields across air gaps. In comparison to mechanical gears, they offer numerous advantages: noise-free operation, reduced vibration, low maintenance, built-in overload protection, and zero backlash[1–4]. As a result, magnetic gears (MGs) are preferred in industries such as wind energy[1, 2, 5] and electric vehicles[6], where there is a growing demand for efficient and reliable energy solutions. Broadly, magnetic gears are classified into two types: those that mimic traditional gears by substituting iron teeth with alternating permanent magnet N-S poles and flux-modulated types [7].

Recently, numerous designs of flux-modulated MGs have emerged, such as linear, axial, harmonic, and planetary designs, all operating by the principles of magnetic field modulation[8-12]. Among these, coaxial magnetic gears are widely used owing to their high torque density and low torque ripple, which makes them suitable for high-performance transmission applications. Moreover, the implementation of Halbach arrays has improved the torque transmission performance of the CMGs while reducing torque ripple[13-15]. Subsequent research employs various methodologies to enhance the torque density of CMGs, including the utilization of high-performance permanent magnet materials (NdFeB)[9] and the innovation of topology design alongside the optimization of design parameters[16–22]. Furthermore, integrating CMGs with other electrical machine components, including in generators, serves as a method to reduce weight and volume, thereby achieving high torque density[11, 22].

Understanding magnetic field behaviour in air gaps is the prior step in evaluating the electromagnetic torque performance of electrical machines, including CMGs[20]. Two broadly used methods for assessing the electromagnetic torque and field behavior of the CMGs are finite element analysis (FEA) and analytical methods. FEA precisely handles geometries and material nonlinearity, whereas analytical methods provide a reliable and efficient solution at the initial design phase[16,22]. Furthermore, the subdomain analytical technique emerged as an effective method to investigate the magnetic field and electromagnetic torque transmission of CMGs[18]. In this research subdomain, the analytical method involves separating variables. This method divides the CMG into subsections and enables solving the formulated partial

---

*Corresponding author (E-mail:ambirewondimu@gmail.com) differential equations (PDEs) derived from Maxwell's equations. The method applies boundary and continuity conditions using Laplacian or Poisson's equations, depending on the material properties and availability of free current for each subsection, which enables precise analysis of electromagnetic torque and magnetic flux.

Despite significant advancements, challenges remain in the topology of coaxial magnetic gear designs, particularly regarding magnetic losses, permanent magnet consumption, volume, susceptibility to rust, and performance consistency. In this context, this study introduces a novel CMG tailored for applications requiring efficient torque and speed transmission. The proposed design incorporates loss mitigation techniques, segments the PMs, and integrates electrical steel sheet supports within a newly developed comb-shaped outer rotor yoke to minimize flux leakage and enhance rust protection. Additionally, an innovative magnetic field modulation pole piece is introduced to suppress flux leakage.

In line with these objectives, a subdomain analytical approach is used to develop the governing equations for characterizing the magnetic torque and magnetic field of the proposed design. After verification through FEA, the novel CMG design is compared with an equivalent CMG used in a wind energy application.

The structure of the manuscript is as follows: It begins with a theoretical formulation that derives key equations for the proposed CMG model, followed by FEA and a presentation of the results along with their relevance. Additionally, the discussion incorporates the proposed model within a compact wind energy system to evaluate its performance further and validates it by comparing the results to those from both 3D and 2D FEA simulations. Finally, the paper concludes with a summary of the main findings and provides suggestions for future research directions.

2 Materials and Methods

As illustrated in Fig. 1, the novel coaxial magnetic gear features three cylindrical elements: the high-speed rotor (1), the stationary ferromagnetic modulating poles (2), and the low-speed rotor (3). This configuration enables the two rotors to spin in opposite directions while the modulating poles remain fixed. The simplified CMG shown in Fig. 2, which is segmented into five sections: the modulator area (i), the inner yoke permanent magnet section (I), the inner air space (II), the outer air space (III), and the portion of the outer yoke that integrates the permanent magnets (IV).

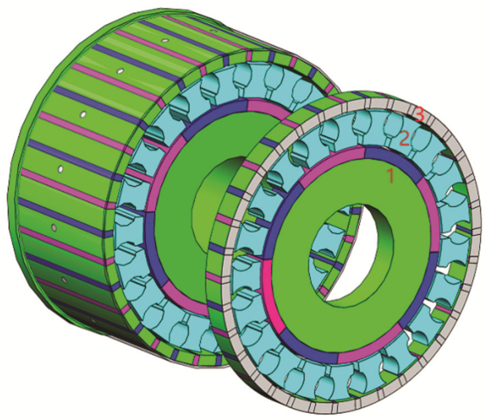

Fig. 1 — Topology of the new CMG, (a) Inner rotor (1), (b) New modulator (2) and (c) New comb shape outer rotor (3).

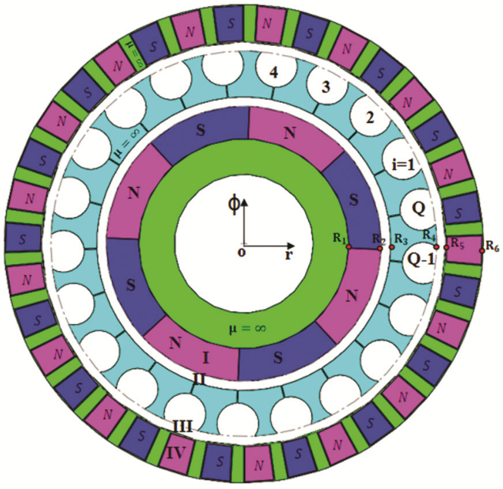

Fig. 2 — Simplified 2D model of new CMG.

2.1 Theoretical formulation

The analytical formulation of the governing equations for the magnetic field and torque in the proposed CMG model is based on the following assumptions.

(a) PM permeability considered one.

(b) Iron yokes permeability is considered infinite.

(c) End effects and eddy current effects are ignored.

Together with assumptions made, magnetic vector potential is solely aligned and exclusively dependent on the r and ϕ cylindrical coordinates.

Modulator slot opening angle (α) for the i^th^ modulator given as:

$$\phi_i = \frac{2\pi i}{Q} + \phi_0 - \frac{\alpha}{2} \quad \text{with } 1 \le i \le Q \qquad \ldots(1)$$

where, $\emptyset_o$ represents the modulator segment's starting angular orientation, which is set to zero, and Q signifies the number of modulators.

This analysis employs partial differential equations, particularly Laplace's equation, to address both the modulator and air subdomains. The separation of variables method (SVM) is employed to solve these equations, providing a comprehensive framework for examining how changes in key design variables influence the performance of the new CMG.

$$P_w(u,v) = \left(\frac{u}{v}\right)^{w} + \left(\frac{v}{u}\right)^{w} \qquad \ldots(2)$$

$$E_w(u,v) = \left(\frac{u}{v}\right)^{w} - \left(\frac{v}{u}\right)^{w} \qquad \ldots(3)$$

2.1.1 Modulator design

Modulator design in a CMG is crucial for improving torque transmission by optimizing the interaction between PMs and soft magnetic materials. This aspect must be carefully considered during the initial design phase of the new model.

The i^{th} subsection of the modulator and its corresponding boundary condition (BC) are illustrated in Fig. 3 as $A^i = A^i(r, \emptyset)$. Laplace's equations in the region defined by the radius R_3 and R_4, constrained by the angular positions $\emptyset_i$ and $\emptyset_i + \alpha$, are given as:

$$\frac{\partial^2 A^i}{\partial r^2} + \frac{1}{r}\frac{\partial A^i}{\partial r} + \frac{1}{r^2}\frac{\partial^2 A^i}{\partial \phi^2} = 0 \ \text{ for} \begin{cases} R_3 \le r \le R_4 \\ \phi_i \le \phi \le \phi_i + \alpha \end{cases} \qquad \ldots(4)$$

The BC for the i^{th} modulator sections are given as:

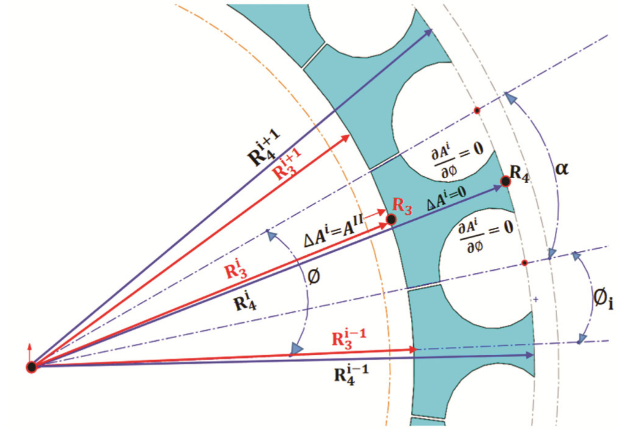

Fig. 3 — Boundary condition for the i^{th} modulator subdomain ($\phi_o = 0$).

$$\left.\frac{\partial A^i}{\partial \phi}\right|_{\phi=\phi_i} = 0 \ \text{ and } \left.\frac{\partial A^i}{\partial \phi}\right|_{\phi=\phi_i+\alpha} = 0 \qquad \ldots(5)$$

Between the air gap section and the i^{th} modulator, the normal component of the flux density remains consistent. as indicated below.

$$A^i(R_3, \phi) = A^{II}(R_3, \phi) \qquad \ldots(6)$$

$$A^i(R_4, \phi) = A^{III}(R_4, \phi) \qquad \ldots(7)$$

From Eq. 4, the general solution obtained using SVM can be expressed as:

$$A^i(r,\phi) = A^i_o + B^i_o \mathrm{In}r + \sum_{k=1}^{\infty}\left(A^i_k r^{-\frac{k\pi}{\alpha}} + B^i_k r^{\frac{k\pi}{\alpha}}\right) \bullet \cos\left(\frac{k\pi}{\alpha}(\phi - \phi_i)\right) \qquad \ldots(8)$$

where as A_0^i, B_0^i, A_k^i and B_k^i are constants. By considering the continuity constraints stipulated in Eqs. 6 and 7, the expression for the vector potential in the i^{th} modulator section is obtained, as follows:

$$A^i(r,\phi) = A^i_o + B^i_o \mathrm{In}r + \sum_{k=1}^{\infty}\Big(A^i_k \frac{E_{k\pi/\alpha}(r,R_4)}{E_{k\pi/\alpha}(R_3,R_4)} - B^i_k \frac{E_{k\pi/\alpha}(r,R_4)}{E_{k\pi/\alpha}(R_3,R_4)} \bullet \cos\left(\frac{k\pi}{\alpha}(\phi - \phi_i)\right) \qquad \ldots(9)$$

where k is natural number, $E_{k\pi/\alpha}(r, R_4)$ is stated on Eq. 3.

Fourier expansion of the vector potentials for both air gap regions$A^{II}(R_3, \emptyset)$and $A^{III}(R_4, \emptyset)$is utilized to obtain the constants A_0^i, B_0^i, A_k^i and B_k^i, which are subsequently applied over the defined interval $(\emptyset_i, \emptyset_i + \alpha)$.

$$A_o^i + B_o^i \mathrm{In}R_3 = \frac{1}{\alpha}\int_{\phi_i}^{\phi_i+\alpha} A^{II}(R_3,\phi) \bullet d\phi \qquad \ldots(10)$$

$$A_o^i + B_o^i \mathrm{In}R_4 = \frac{1}{\alpha}\int_{\phi_i}^{\phi_i+\alpha} A^{III}(R_4,\phi) \bullet d\phi \qquad \ldots(11)$$

$$A_k^i = \frac{2}{\alpha}\int_{\phi_i}^{\phi_i+\alpha} A^{II}(R_3,\phi)\cos\left(\frac{k\pi}{\alpha}(\phi - \phi_i)\right)d\phi \qquad \ldots(12)$$

$$B_k^i = \frac{2}{\alpha}\int_{\phi_i}^{\phi_i+\alpha} A^{III}(R_4,\phi)\cos\left(\frac{k\pi}{\alpha}(\phi - \phi_i)\right)d\phi \qquad \ldots(13)$$

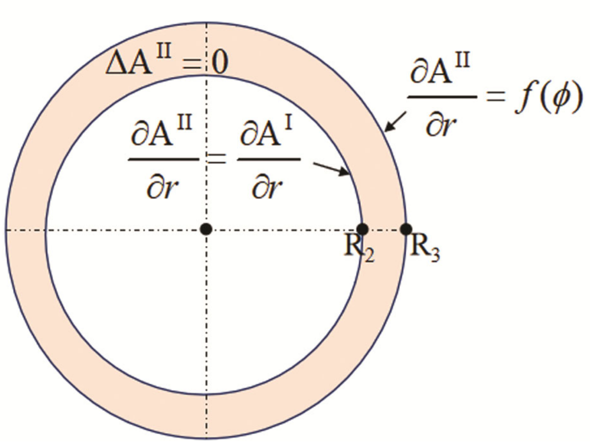

Fig. 4 —Inner air gap at boundary (R_2, R_3).

2.1.2 Inner air gap

Based on the novel CMG design arrangement illustrated in Fig. 2, section II shows the inner air gap, along with corresponding BC depicted through the annular cross-section of Fig. 4 as $A^{II}=A^{II}(r,\varnothing)$. Laplace's equation can be applied in this region and solved as follows:

$$\frac{\partial^2 A^{II}}{\partial r^2}+\left(\frac{1}{r}\right)\frac{\partial A^{II}}{\partial r}+\left(\frac{1}{r^2}\right)\frac{\partial^2 A^{II}}{\partial \phi^2}=0 \text{ for}\begin{cases}R_2 \le r \le R_3\\ 0 \le \phi \le 2\pi\end{cases} \quad \ldots(14)$$

The continuity equation provides the following value for the tangential magnetic field at $r = R_2$:

$$\left.\frac{\partial A^{II}}{\partial r}\right|_{r=R_3} = \left.\frac{\partial A^{I}}{\partial r}\right|_{r=R_2} \quad \ldots(15)$$

The presence of slots at the boundary condition $r = R_3$ complicates its formulation. To establish the boundary condition, the magnetic field at the boundary adjacent to the slots and the air region is utilized as follows:

$$\left.\frac{\partial A^{II}}{\partial r}\right|_{r=R_3} = f(\phi) \quad \ldots(16)$$

whereas:

$$f(\phi)=\begin{cases}\left\{\left.\frac{\partial A_i}{\partial r}\right|_{r=R_3}\right. & \forall \phi \in \left[\phi_i, \phi_i+\alpha\right]\\ 0 & \text{else where}\end{cases} \quad \ldots(17)$$

Where $A^i(r,\varnothing)$ is the vector potential in the i^{th} modulator defined in Eq. 9. General solution of Eq.14 is obtained from the Sturm-Liouville problem applied to Fig. 4. The vector potential can be calculated by applying the boundary conditions from Eqs. 15 & 16, which are expressed as:

$$\begin{aligned}&A^{II}(r,\phi)=A^{II}_{o}\\&+\sum_{k=1}^{\infty}\left(A^{II}_{n}\left(\frac{R_2}{n}\right)\left(\frac{P_n(r,R_3)}{E_n(R_2,R_3)}\right)+B^{II}_{n}\left(\frac{R_3}{n}\right)\left(\frac{P_n(r,R_2)}{E_n(R_3,R_2)}\right)\right)\cos(n\phi)\\&+\sum_{k=1}^{\infty}\left(C^{II}_{n}\left(\frac{R_2}{n}\right)\left(\frac{P_n(r,R_3)}{E_n(R_2,R_3)}\right)+D^{II}_{n}\left(\frac{R_3}{n}\right)\left(\frac{P_n(r,R_2)}{E_n(R_3,R_2)}\right)\right)\sin(n\phi)\end{aligned} \quad \ldots(18)$$

whereas n-is natural number. Through the elaboration of Fourier formulation of $\left.\frac{\partial A^{I}}{\partial r}\right|_{R_2}$ and $f(\varnothing)$ across[0, 2π], all coefficients are obtained as follows:

$$A^{II}_{n}=\frac{2}{2\pi}\int_0^{2\pi}\left.\frac{\partial A^{I}}{\partial r}\right|_{R_2}\bullet\cos(n\phi)\,d\phi \quad \ldots(19)$$

$$B^{II}_{n}=\frac{2}{2\pi}\int_0^{2\pi}f(\phi)\bullet\cos(n\phi)\,d\phi \quad \ldots(20)$$

$$C^{II}_{n}=\frac{2}{2\pi}\int_0^{2\pi}\left.\frac{\partial A^{I}}{\partial r}\right|_{R_2}\bullet\sin(n\phi)\,d\phi \quad \ldots(21)$$

$$D^{II}_{n}=\frac{2}{2\pi}\int_0^{2\pi}f(\phi)\bullet\sin(n\phi)\,d\phi \quad \ldots(22)$$

The Neumann problem associated with Equations 14, 15, and 16 can be solved when this condition is satisfied:

$$\int_0^{2\pi}\left.\frac{\partial A^{I}}{\partial r}\right|_{R_2}\bullet d\phi=\int_0^{2\pi}f(\phi)\bullet d\phi \quad \ldots(23)$$

Simplifying Eq. 23 results in the following relationships among the coefficients B^i_o defined in Equations 10 and 11.

$$\sum_{i=1}^{Q}B^{i}_{o}=0 \quad \ldots(24)$$

The magnetic flux density is computed as follows:

$$B_{IIr}=\left(\frac{1}{r}\right)\frac{\partial A^{II}}{\partial \phi} \quad \ldots(25)$$

$$B_{II\phi}=(-1)\frac{\partial A^{II}}{\partial r} \quad \ldots(26)$$

The formula is used to calculate the flux density in the tangential and radial sections of the air space region:

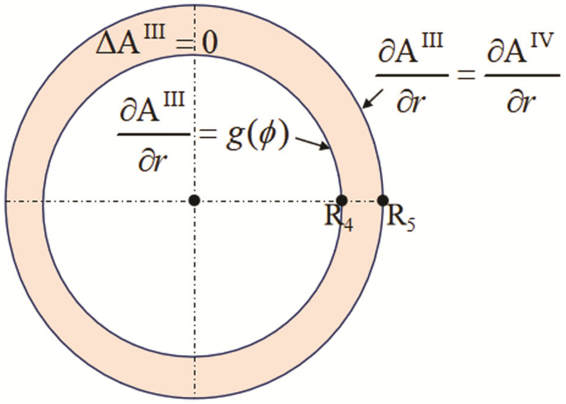

Fig. 5 — Outer air-gap model at boundary (R_4, R_5).

$$B_{IIr}(r,\phi) = +\sum_{n=1}^{\infty} -\left(A^{II}{}_{n}\left(\frac{R_2}{r}\right)\left(\frac{P_n(r,R_3)}{E_n(R_2,R_3)}\right) + B^{II}{}_{n}\left(\frac{R_3}{r}\right)\left(\frac{P_n(r,R_2)}{E_n(R_3,R_2)}\right)\right)\sin(n\phi) + \sum_{n=1}^{\infty}\left(C^{II}{}_{n}\left(\frac{R_2}{r}\right)\left(\frac{P_n(r,R_3)}{E_n(R_2,R_3)}\right) + D^{II}{}_{n}\left(\frac{R_3}{r}\right)\left(\frac{P_n(r,R_2)}{E_n(R_3,R_2)}\right)\right)\cos(n\phi) \quad \ldots(27)$$

$$B_{II\theta}(r,\phi) = +\sum_{n=1}^{\infty} -\left(A^{II}{}_{n}\left(\frac{R_2}{r}\right)\left(\frac{P_n(r,R_3)}{E_n(R_2,R_3)}\right) + B^{II}{}_{n}\left(\frac{R_3}{r}\right)\left(\frac{P_n(r,R_2)}{E_n(R_3,R_2)}\right)\right)\cos(n\phi) + \sum_{n=1}^{\infty} -\left(C^{II}{}_{n}\left(\frac{R_2}{r}\right)\left(\frac{P_n(r,R_3)}{E_n(R_2,R_3)}\right) + D^{II}{}_{n}\left(\frac{R_3}{r}\right)\left(\frac{P_n(r,R_2)}{E_n(R_3,R_2)}\right)\right)\sin(n\phi) \quad \ldots(28)$$

2.1.3 Outer air gap

According to Fig. 2, region III corresponds to the outer air gap, along with the relevant BC illustrated in the annular cross-section in Fig. 5, as $A^{III} = A^{III}(r, \emptyset)$.

In this section, magnetic flux density is investigated using Laplace's formulation:

$$\frac{\partial^2 A^{III}}{\partial r^2} + \left(\frac{1}{r}\right)\frac{\partial A^{III}}{\partial r} + \left(\frac{1}{r^2}\right)\frac{\partial^2 A^{III}}{\partial \phi^2} = 0 \quad \text{for}\begin{cases} R_4 \le r \le R_5 \\ 0 \le \phi \le 2\pi \end{cases} \quad \ldots(29)$$

For this section, the boundary condition at r = R_5 is given as:

$$\left.\frac{\partial A^{III}}{\partial r}\right|_{r=R_5} = \left.\frac{\partial A^{IV}}{\partial r}\right|_{r=R_5} \quad \ldots(30)$$

Similarly, the BC when the radius is r = R_4 can also be stated as:

$$\left.\frac{\partial A^{III}}{\partial r}\right|_{r=R_4} = g(\phi) \quad \ldots(31)$$

With

$$g(\phi) = \begin{cases} \left\{\left.\frac{\partial A_i}{\partial r}\right|_{r=R_4}\right. & \forall \phi \in [\phi_i,\ \phi_i + \alpha] \\ 0 & \text{else where} \end{cases} \quad \ldots(32)$$

The vector potential in this section is obtained by applying the boundary conditions from Eqs. 30 & 31, as follows:

$$A^{III}(r,\phi) = A_o{}^{III} + \sum_{n=1}^{\infty}\left(A_n{}^{III}\left(\frac{R_4}{n}\right)\left(\frac{P_n(r,R_5)}{E_n(R_4,R_5)}\right) + B_n{}^{III}\left(\frac{R_5}{n}\right)\left(\frac{P_n(r,R_4)}{E_n(R_5,R_4)}\right)\right)\cos(n\phi) + \sum_{n=1}^{\infty}\left(C_n{}^{III}\left(\frac{R_4}{n}\right)\frac{P_n(r,R_5)}{E_n(R_4,R_5)} + D_n{}^{III}\left(\frac{R_5}{n}\right)\left(\frac{P_n(r,R_4)}{E_n(R_5,R_4)}\right)\right)\sin(n\phi) \quad \ldots(33)$$

where n is natural number, $P_n(r, R_5)$ and $E_n(R_4, R_5)$ are stated on Eqs.2 & 3. The elaboration of Fourier formulation on $\left.\frac{\partial A^{IV}}{\partial r}\right|_{R_5}$ & g(ϕ) across the range [0, 2π], all coefficients are determined as:

$$A_n{}^{III} = \frac{2}{2\pi}\int_0^{2\pi} g(\phi) \bullet \cos(n\phi)d\phi \quad \ldots(34)$$

$$B_n{}^{III} = \frac{2}{2\pi}\int_0^{2\pi} \left.\frac{\partial A^{IV}}{\partial r}\right|_{r=R_5} \bullet \cos(n\phi)d\phi \quad \ldots(35)$$

$$C^{III}{}_{n} = \frac{2}{2\pi}\int_0^{2\pi} g(\phi) \bullet \sin(n\phi)d\phi \quad \ldots(36)$$

$$D^{III}{}_{n} = \frac{2}{2\pi}\int_0^{2\pi} \left.\frac{\partial A^{IV}}{\partial r}\right|_{R_5} \bullet \sin(n\phi)d\phi \quad \ldots(37)$$

2.1.4 Segmented permanent magnets

The outer yoke integrated segmented PMs Section is indicated by superscript IV, with the BC in Fig. 6(a) as $A^{IV} = A^{IV}(r, \emptyset)$. For simplicity, the vector potential of the segmented PMs is modeled as an annular section in Fig. 6(b).

It can also be solved in the following manner:

$$\frac{\partial^2 A^{IV}}{\partial r^2} + \left(\frac{1}{r}\right)\frac{\partial A^{IV}}{\partial r} + \left(\frac{1}{r^2}\right)\frac{\partial A^{IV}}{\partial \phi^2} = \left(\frac{\mu_0}{r}\right)\frac{\partial M_r}{\partial \phi} \quad for\begin{cases} R_5 \le r \le R_6 \\ 0 \le \phi \le 2\pi \end{cases} \quad \ldots(38)$$

The BC of the segmented yoke section at r = R_6 is given as

$$A^{IV}(R_5, \phi) = A^{III}(R_5, \phi) \quad \ldots(39)$$

$$\left.\frac{\partial A^{IV}}{\partial r}\right|_{r=R_6} = 0 \quad \ldots(40)$$

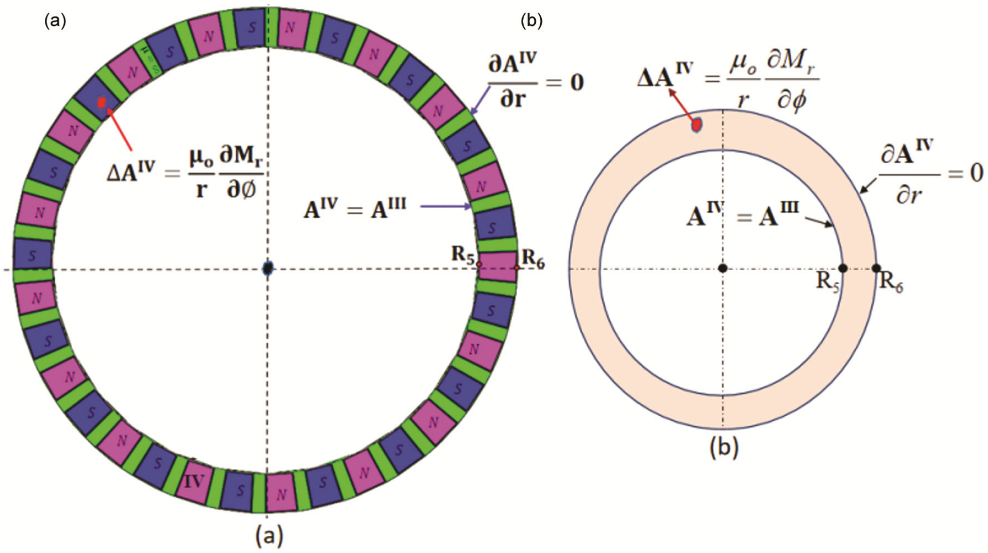

Fig. 6 — Outer segmented PMs integrated iron yoke with its boundary conditions (R_5, R_6) (a) Actual model and (b) Simplified model.

By including the boundary conditions from Eqs. 39 and 40, the magnetic vector potential within the segmented magnets can be represented as follows:

$$\begin{aligned}&A^{IV}(r,\phi)=\\&+\sum_{n=1}^{\infty}\left(A_n^{IV}\left(\frac{P_n(r,R_6)}{P_n(R_5,R_6)}\right)+Y_n(r)\left(\cos(n\phi_0)\right)\right)\bullet\cos(n\phi)\\&+\sum_{n=1}^{\infty}\left(C_n^{IV}\left(\frac{P_n(r,R_6)}{P_n(R_5,R_6)}\right)+Y_n(r)\left(\sin(n\phi_0)\right)\right)\bullet\sin(n\phi)\end{aligned} \quad \ldots(41)$$

where

$$Y_n(r)=\left(1+\frac{1}{n}\left(\frac{R_6}{r}\right)^{n+1}\right)\bullet g_n(r)-\frac{P_n(r,R_6)}{P_n(R_5,R_6)}\left(1+\frac{1}{n}\left(\frac{R_6}{R_5}\right)^{n+1}\right)\bullet g_n(R_5) \quad \ldots(42)$$

$$g_n(r)=\begin{cases}\dfrac{4B_r\bullet r\bullet p_o}{\pi(1-n^2)} & ,\text{if}\Rightarrow n=jp_o\text{ , with } j=1,3,5,\ldots\\ \left(\dfrac{2B_r}{\pi}\right)r\,\mathrm{In}r & ,\text{ if}\Rightarrow n=p_o=1\\ 0 & \Rightarrow\text{otherwise}\end{cases} \quad \ldots(43)$$

where p_o is pole pairs on comb shaped yoke, $P_n(r, R_6)$ is given on Eq.1. Through Fourier series expansion of $A^{III}(R_5, \emptyset)$ across the range [0, 2π] A_n^{IV}, and C_n^{IV} are the coefficients obtained as:

$$A_n^{IV}=\frac{2}{2\pi}\int_0^{2\pi}A^{III}(R_5,\phi)\bullet\cos(n\phi)\bullet d\phi \quad \ldots(44)$$

$$C_n^{IV}=\frac{2}{2\pi}\int_0^{2\pi}A^{III}(R_5,\phi)\bullet\sin(n\phi)\bullet d\phi \quad \ldots(45)$$

2.2 Torque analysis

The torque produced by the magnetic field can be described using the Maxwell tensor by selecting a circular integration path with radii R_i and R_o for the inner and outer air gaps, respectively. Thus, the torque is represented as follows:

$$T_i=\left(\frac{LR_i^{\,2}}{\mu_o}\right)\int_0^{2\pi}B_r^{II}(R_i,\phi)\bullet B_\phi^{II}(R_i,\phi)\,d\phi \quad \ldots(46)$$

$$T_o=\left(\frac{LR_o^{\,2}}{\mu_o}\right)\int_0^{2\pi}B_r^{III}(R_o,\phi)\bullet B_\phi^{III}(R_o,\phi)\,d\phi \quad \ldots(47)$$

where L- is the novel CMG model's stack length.

3 Results and Discussion

3.1 Magnetic flux simulation

The novel CMG was designed in 2D and 3D using the design parameters in Table 1. Finite element analysis was performed using COMSOL multiphysics. To optimize computational time and memory usage, a quarter-symmetry model was employed for the 3D FEA.

Figure 7(a-b) show a finer tetrahedral mesh used for simulating both models, with its quality checked to ensure it falls within the safest range for further analysis.

A rigorous numerical study assessed how varying key design variables, such as air gap and PM thickness, affect the proposed CMG model's

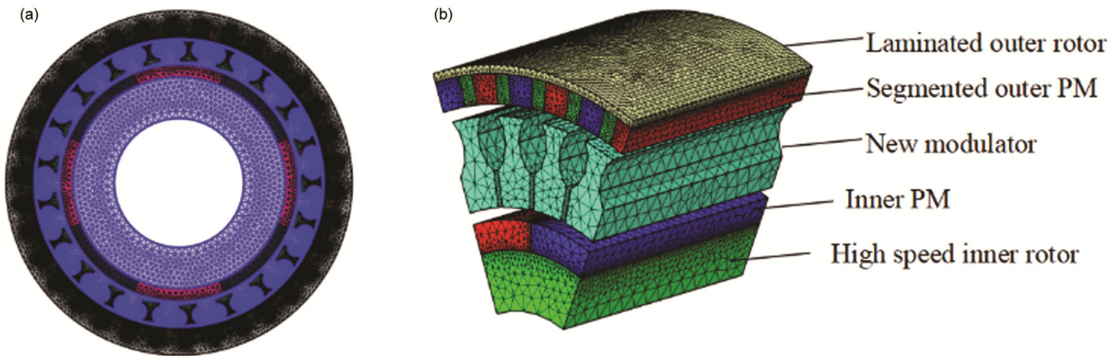

Fig. 7 — Mesh of the (a) 2D and (b) 3D quarter model of CMG.

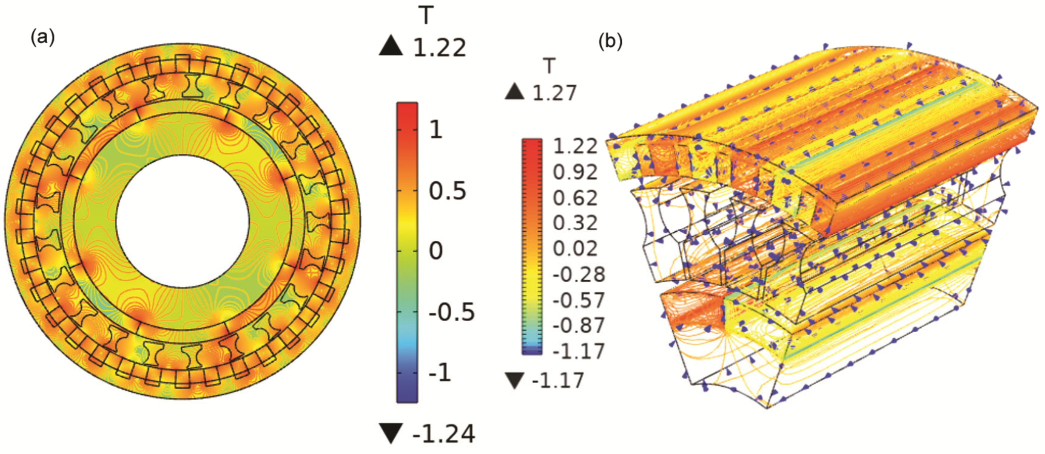

Fig. 8 — Flux distribution (a) 2D, and (b) 3D quarter CMG model.

Table 1 — Coaxial magnetic gear design specifications [1], [7].

Symbols	Parameters	Value
R_1	Interior radius of IR (mm)	20
R_2	Exterior radius of IR (mm)	25
R_3	Pp inner radius (mm)	49
R_4	Pp outer radius (mm)	64
R_5	Interior radius of OR (mm)	65
R_6	Exterior radius of OR (mm)	70
g	Air gap thickness inner/outer (mm)	2
T_m	Thickness of modulator (mm)	15
T_{pm}	PM thickness (mm)	5
N_l	Outer pole pairs	17
N_h	Inner pole pairs	4
N_m	Pole piece	21
L(mm)	Axial length (mm)	60
μ_m (T)	PMs Remanence	1.2

Where: IR (Inner rotor), OR (Segmented outer rotor), Pp (Pole piece)

performance. Figures 8(a-b) illustrate the magnetic flux line distribution, with flux densities of 1.22 T and 1.27 T for the 2D and 3D FEA models, respectively.

Table 2 — Variables for performance metrics.

Parameters	Values
Air gap length (mm)	2, 4,6,8
Permanent magnet thickness (mm)	4,5, 6,8,10

3.2 Parametric study

Air gap length and PM thickness are crucial design factors affecting the performance of the novel CMG model. Table 2 presents the chosen practical design variables that impact the performance of the developed electrical machines, including the CMG model.

The inner and outer air regions are essential for influencing the flux density in the CMG, as demonstrated in Figs 9 (a-d). Higher reluctance leads to a decrease in magnetic flux, which in turn affects its distribution. A smaller air gap improves magnetic flux, while a larger one weakens flux loops and field intensity.

Furthermore, the PM thickness influences the magnetic circuit, enhancing flux flow as the thickness increases, as shown in Figs 10 (a-b).

A smaller air gap enhances magnetic coupling between the PMs, resulting in increased torque, as

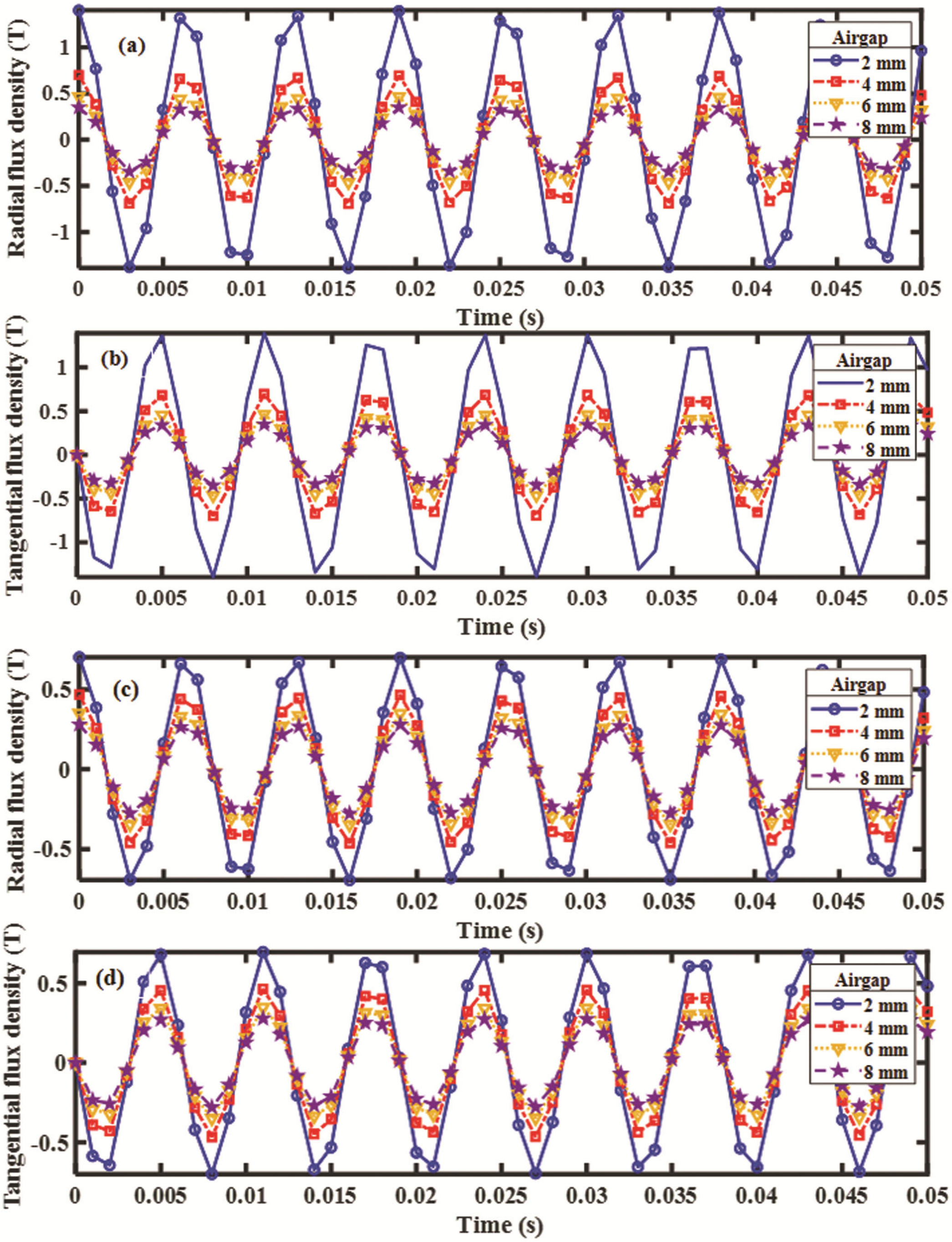

Fig. 9 — Inner (a)-(b) and outer (c)-(d) air gaps vs flux densities plot.

shown in Figs 11 (a-b). In contrast, a larger air gap diminishes torque due to higher reluctance.

3.3 Model validation

Model validation was conducted by comparing the post-processed FEA results with the proposed model using MATLAB 2021. Figure 12 demonstrates that flux density decreases as the air gap increases, with analytical results closely aligning with 3D FEA, while minor discrepancies are observed with 2D FEA due to neglected 3D effects.

Similarly, Fig. 13 indicates that torque decreases with a larger air gap, showing consistent results between the analytical and 3D FEA methods.

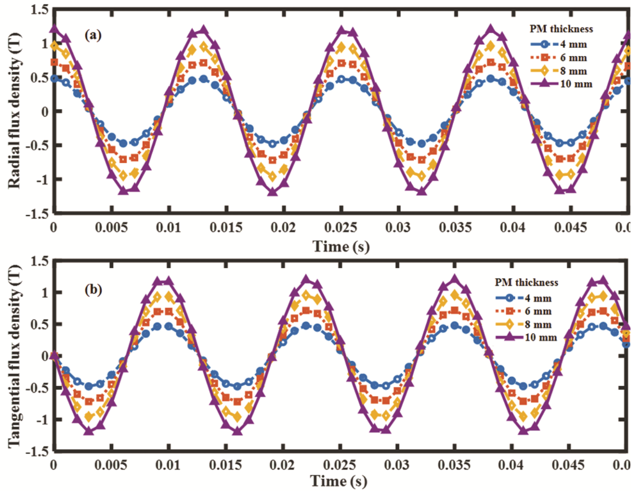

Fig. 10 — Flux distribution (a) Radial, and (b) Tangential.

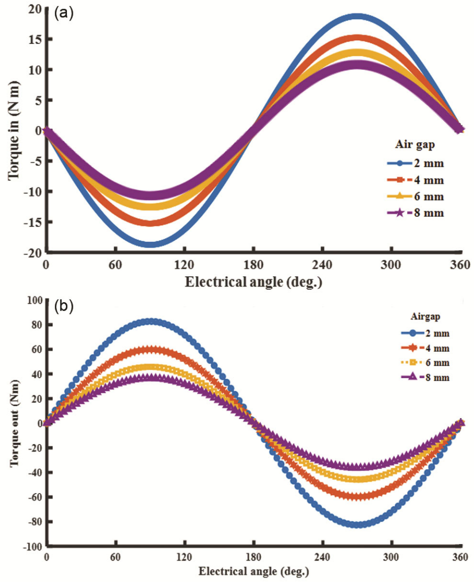

Fig. 11 — (a). Torque in, (b) Torque out plot.

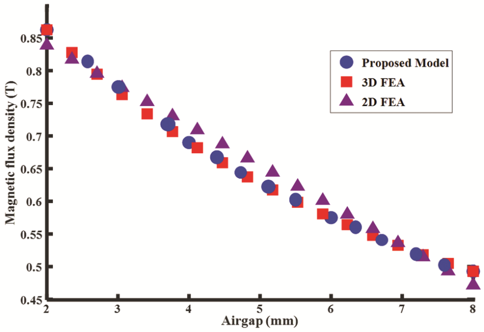

Fig. 12 — Verification curve of flux density versus air gap.

Figure 14 confirms the impact of PM thickness on torque performance, revealing a strong correlation between the proposed model and both 2D and 3D FEA outcomes.

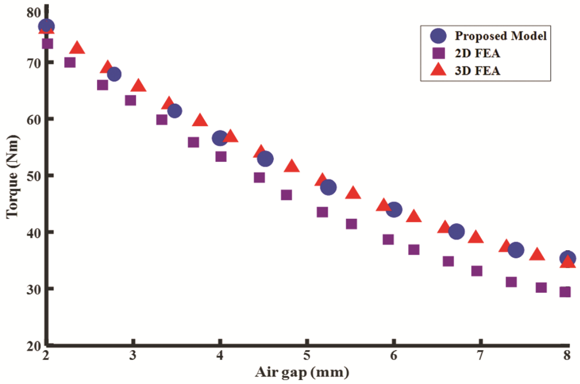

Fig. 13 — Verification curve of torque out versus air gap.

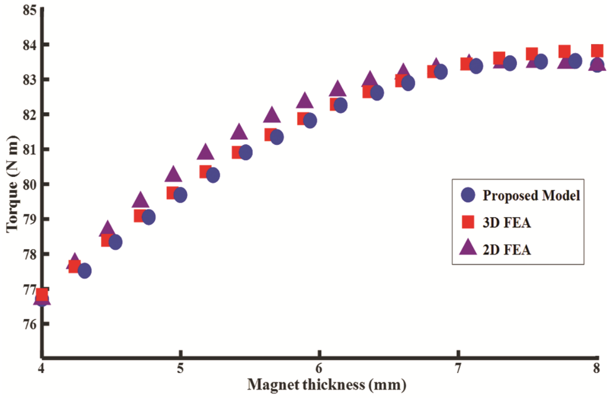

Fig. 14 — Verification curve of torque versus PM thickness.

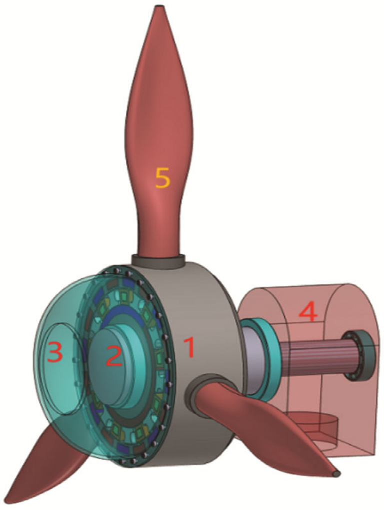

Fig. 15 — Application of the new CMG for small-scale wind turbines. (a). CMG (1), (b). Shaft with bearing support (2), (c). Fairing cover (3), (d). Power electronics house (4), and (e) Turbine blades (5).

The proposed CMG model is integrated into the transmission system of a small-scale domestic wind turbine application, as shown in Fig. 15.

3.3.1 Application

Based on Fig. 15, a performance comparison is conducted between the new CMG designs and existing model for small-scale wind turbines, based on the specifications listed in Table 1. All analysis conditions remain consistent, except for the new topology, which features a modulator and a comb-shaped outer yoke with segmented PMs. The flux density increased by 1.05% in the interior air space and by 3.2% in the exterior space, as illustrated in Figs 16(a–d).

Additionally, Fig. 17 reveals a rise in torque of 1.36% for the inner region and 2.06% for the outer region. Furthermore, the segmentation of permanent magnets and the comb-shaped outer yoke reduce volume and weight, enabling easier integration and

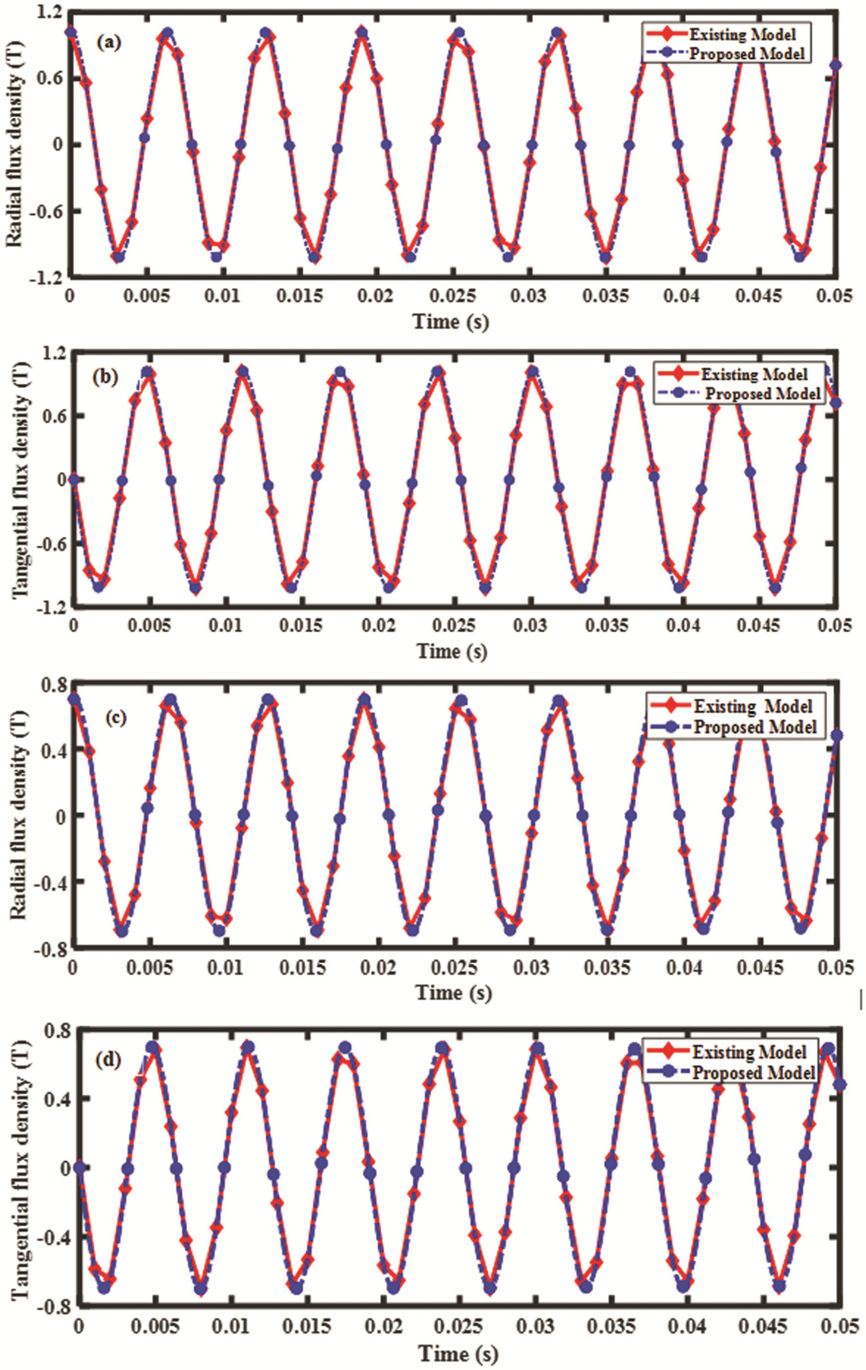

Fig. 16 — Comparison of inner (a-b) and outer (c-d) air gap flux densities.

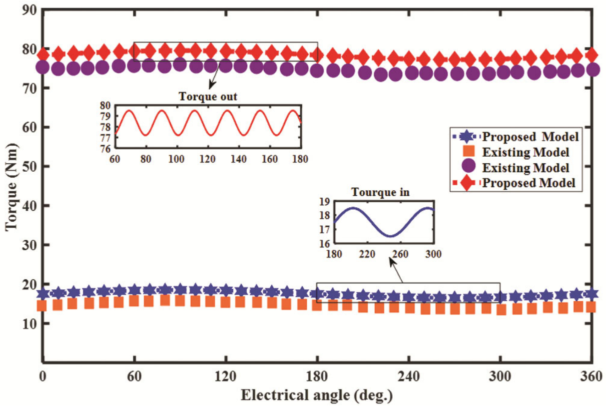

Fig. 17 — Comparison of dynamic torque.

minimizing material use. This design presents a more sustainable and effective solution, advancing wind turbines and high-performance magnetic transmission applications, including electric vehicles.

4 Conclusion

This research presents a design, analytical, and FEA-based study of a novel CMG design that features a ferromagnetic pole piece, a comb-shaped outer yoke, and an electrical steel sheet for back support. The magnetic torque and flux density equations are derived using the analytical subdomain method, which is based on the new topology. This method integrates boundary and continuity conditions while considering material and geometric nonlinearity. Additionally, Poisson's and Laplace's equations are applied to the relevant subsections.

The proposed results of the analysis, validated through both 2D and 3D FEA, show strong consistency in magnetic torque and flux density results. The 3D FEA results indicate less than 5% deviation for magnetic flux and less than 3% deviation for magnetic torque, underscoring the accuracy of the model analysis. Furthermore, the new design achieves an improvement of 2.06% in magnetic torque and 3.2% in magnetic flux density compared to a conventional design. These advancements point out the potential of this newly developed CMG design to transform high-performance applications in magnetic transmission.

References

1 K Atallah & D Howe, *IEEE Tran Magn,* 37(2001) 4.
2 X Shen, Y Li, H Hao& J Jin, *IEEE Trans Ene Convers*, 32 (2017) 267.
3 M Johnson, et al., *IEEE TransInd Appl*, 54(2018) 4.
4 T Lubin, S Mezani & A Rezzoug, *IEEE Trans Magn,* 49(2013) 5507.
5 C Wu & S Jian, *Appl Math Modelling*, 39(2015) 5746.
6 J. Ding, et al. 58(2022) 1.
7 Yang C, et al., *Ind JEng Mater Sci*, 31(2024) 475.
8 R Bharani & A Sivaprakasam, *IETE J Res*, 68(2020) 3341.
9 H Zhao & Z Song, *IEEE Tran Ind Appl,* 57(2021)1.
10 Y Wang, et al. 55(2019) 3445.
11 R Benlamine, et al., *IEEE Int Conf on Elect Machines in Switzerland*, (2016) 1888.
12 L Jing, et al, *IEEE Trans Appl Supercond,* 33(2023) 1.
13 Jian L. Chau KT., *IEEE Trans.Energy con*., 25(2010) 319.
14 M Amin Masoudi & A Afsari, *IEEE Access,* 12(2024) 81067.
15 M Nguyen et al., *Machines*, 11(2023) 887.
16 L Jing, J Gong, Z Huang, T Ben, & Y Huang, *IEEE Access,* 7 (2019) 75550.
17 E Lee, H Song, J Jeong & S Jeong, *IEEE Robot Autom Lett,* 7(2022) 3357.
18 M Gardner, E Jack, M Johnson& A Toliyat, *IEEE Trans Ind Appl*, 54(2018) 3305.
19 B Yan, et al., *IET Electric Power Appl,* 18(2024) 1.
20 Praslicka B, Gardner MC, Johnson M, Toliyat HA, *IEEE J Emerg Sel Top Power Electron,* 10(2022) 181.
21 X Liu, Y Zhao, M Lu, Z Chen & S Huang, *IEEE Trans Magn*, 57(2021) 1.
22 Yang C, et al., *IETE J Res,* 70(2024) 8580.